33RD CONGRESS
OF THE INTERNATIONAL COUNCIL
OF THE AERONAUTICAL SCIENCES
STOCKHOLM, SWEDEN, 4-9 SEPTEMBER, 2022

ICAS 2022 SWEDEN

NUMERICAL AND EXPERIMENTAL INVESTIGATIONS ON THE DLR-F23 COMBAT AIRCRAFT WIND TUNNEL MODEL

J. Zastrow[†], F. Oberdieck[§], U. Henne[¶] & C. Klein[‖]

German Aerospace Center (DLR) - Göttingen

Abstract

Most combat aircraft with multiple swept leading edges exhibit rapid vortical flow topology evolution and intense flow unsteadiness throughout their flight regime. Some associated phenomena are vortex-interactions, vortex-shock interactions and vortex breakdown.
Accordingly, a combat aircraft's flight control system must regulate the flow behavior differently for many combinations of Mach-number, angle of incidence, angle of sweep, turn radius, etc. As a consequence, understanding the fluid mechanical mechanisms of stabilizing or destabilizing local flow topologies is a key element for an effective control design. Even though this has been known for decades, this subject remains a driving challenge during the design of new combat aircraft.
This raises the question, how the needed aerodynamic data may be retrieved and evaluated better. As a baseline, this task asks for complementary data sets, which combine global forces and dynamics with well resolved local flow features. As an outcome, these data sets yield the characterization of topological features in global and local scales and their impact on the aerodynamic forces. However, only a good temporal resolution will enable the formulation of transfer functions between these flow features, and thereby enable a stability analysis.
In order to address this subject, the *DLR-F23* was developed. The research on this model combines wind tunnel experiments and CFD-calculations. The experiments are conducted in the *Transonic Wind Tunnel Göttingen* with Mach-numbers 0.5 up to 1.2 and angles of incidence between $0°$ and $30°$. The measurement equipment comprises a six-component piezo-electric balance, acceleration sensors, unsteady pressure transducers on the models suction side, wind tunnel wall pressures and time-resolved pressure sensitive paint. Next to a sampling rate of up to $30kHz$, a key element is, that all data acquisition is time-synchronized. On the numerical side, the DLR-TAU code flow solver provides high-fidelity data, which can either complement or extend the experiment. With this data at hand, the flow topology evolution, as well as the inherent unsteady effects can be investigated on.

Keywords: Double Delta, Multi-Vortex System, Large Amplitude Maneuver, Hybrid-RANS-LES

Nomenclature

α	=	angle of attack / incidence
α_0	=	initial angle of attack at start of measurement
β'	=	profile angle
δ_{99}	=	boundary layer height
λ	=	sweep angle
$\sigma(cp)$	=	standard deviation pressure coefficient
cp_{mean}	=	mean of pressure coefficient
c_{my}	=	pitching momentum coefficient
F_s	=	sampling frequency
Ma_δ	=	Mach-number in the boundary layer
t_{mnv}	=	time of maneuver

[†]Institute of Aeroelasticity, jonas.zastrow@dlr.de
[§]DLR Engineering Department (SHT), frank.oberdieck@dlr.de
[¶]Institute for Aerodynamics and Flow Technology, ulrich.henne@dlr.de
[‖]Institute for Aerodynamics and Flow Technology, christian.klein@dlr.de

t_{msr}	=	time of measurement
DNW	=	German-Dutch wind tunnels
CFD	=	computational fluid dynamics
CWT	=	continuous wavelet transform
$(ea)RSM$	=	(explicit algebraic) Reynolds-stress model
HPC	=	high performance computing
$IDDES$	=	improved delayed detached eddy simulation
$iPSP$	=	time-resolved pressure sensitive paint
MAC	=	mean aerodynamic chord
POD	=	proper orthogonal decomposition
PSD	=	power spectral density
SHT	=	Systemhaus Technik
$(u)RANS$	=	(unsteady) reynolds-averaged Navier-Stokes

1. Introduction

Intense research effort has been invested into the understanding of vortical flow behaviour throughout the last decades [1–5]. Usually, combat aircraft feature delta wings, that create strong lift- and momentum-derivatives through a dedicated vortex system. The topological features of this vortex system evolve constantly with changes in Mach-number and changes in angle of incidence (α). Additionally, the inherent unsteadiness of the flow increases and decreases throughout the flight regime as well. There are for example large scale phenomena such as vortex-shock interactions, feeding sheet tearing, vortex breakdowns and on double delta wings additionally vortex-vortex interactions [6–8]. Furthermore, the vortex-system might interact with the aircraft structure, which can lead from the various stages of buffeting up to structural failure. Consequently, the benefits of vortical flow may only be exploited to their full extend, when the sources of stability and instability within these flow structures are understood and managed accordingly.

It has become a standard in this research field, to combine experimental and numerical methods. Also, it has been shown a number of times, that current CFD-capabilities suffice to reproduce flow topologies seen in experiments [9–14]. Nevertheless, accurate CFD-simulations are still demanding. Especially, the reproduction of the unsteady flow phenomena within the frequency domain has its challenges [15, 16]. On the one hand, the computational effort of time-accurate CFD (high fidelity) is one to two orders of magnitude higher than spatial-accurate CFD (low to mid-fidlity). On the other hand, experiments must be designed thoroughly in order to be complemented and extended by numerical simulations effectively. This means not only, that the installation of many sensors and high sampling rates, but furthermore that all data need to be synchronized in time, which includes the tracking of time-resolved boundary conditions. All in all, these requirements should enable an in-depth analysis of vortex flow stability and instability mechanisms.

Having stated that, the current DLR-project *Diabolo* (2018-2023) provides a data base of this kind already and aims to develop the corresponding analysis techniques. This project carries on the legacy of many preceding research campaigns, that all focused on different aspects of combat aircraft design. *Diabolo* comprises a new model family of combat aircraft wind tunnel models. One of these is the pitch-actuated *DLR-F23* semi-span model, which is the object of the presented work. In addition to that, there is the *DLR-F22* modular full-span model [17], which became the baseline design for the DLR-FFD (future fighter demonstrator).

The current work reviews the first wind tunnel test campaign and shows the unsteadiness of the global forces and moments throughout the experimental range. Furthermore, the Mach-number effect vortex de-twining is demonstrated on behalf of time-resolved pressure sensitive paint. Additionally, the flow toplogies and the frequency content of high fidelity CFD-results is compared with experimental data.

2. The Wind Tunnel Experiment

As will be described, the model planform and shape is mostly generic and derived by literature. In particular, the *DLR-F23* represents the initial design of the new *Diabolo* wind tunnel model family, which was introduced in 2018. A rough validation of the desired flow topologies was provided by RANS calculations and first results were presented in 2019 [18]. After the introduction of the HPC-cluster Cara, the placement of the unsteady pressure transducers and aerodynamic loads for the structural design of the wind tunnel model could be accompanied by more demanding CFD-calculations. In detail,

the numerical procedure employed an eaRSM-turbulence model for RANS and a RSM-turbulence model for uRANS. Additionally, the numerical grids were locally refined by solution-based grid adaptation [19]. In parallel, constructional modifications realized the compatibility between the hydraulic pitch actuation test rig and the perforated test section of the *Transonic Wind Tunnel Göttingen*. Eventually, the first wind tunnel experiments were launched in December 2021 and finished in the end of January 2021.

2.1 DLR-F23 Planform and Shape

The planform can be described as a $45°/75°$ double delta with enlarged diamond fillet and ogival cosine-chined forebody [20–26]. Furthermore, the model incorporates elliptic profiles [27], that taper into a sharp trailing edge of $0.5mm$ height and into a constant radius of $0.5mm$ at the leading edges. In fact, the design aims to place the secondary vortices close to the leading edge, so tertiary vortices are suppressed and vorticity redistribution to the primary vortex is maximized [28–30]. Also, the local profile thickness tapers in span-wise direction down to a thickness of $7mm$ at the cropped wing tips (see Fig. 1). All in all, there are four leading edges, that produce each their own primary separation:

- $45°$ main wing $:= MW$
- diamond fillet ($45°$ levcon, $75°$ strake) $:= DF$ (DF_L, DF_S)
- ogival forebody $:= OF$

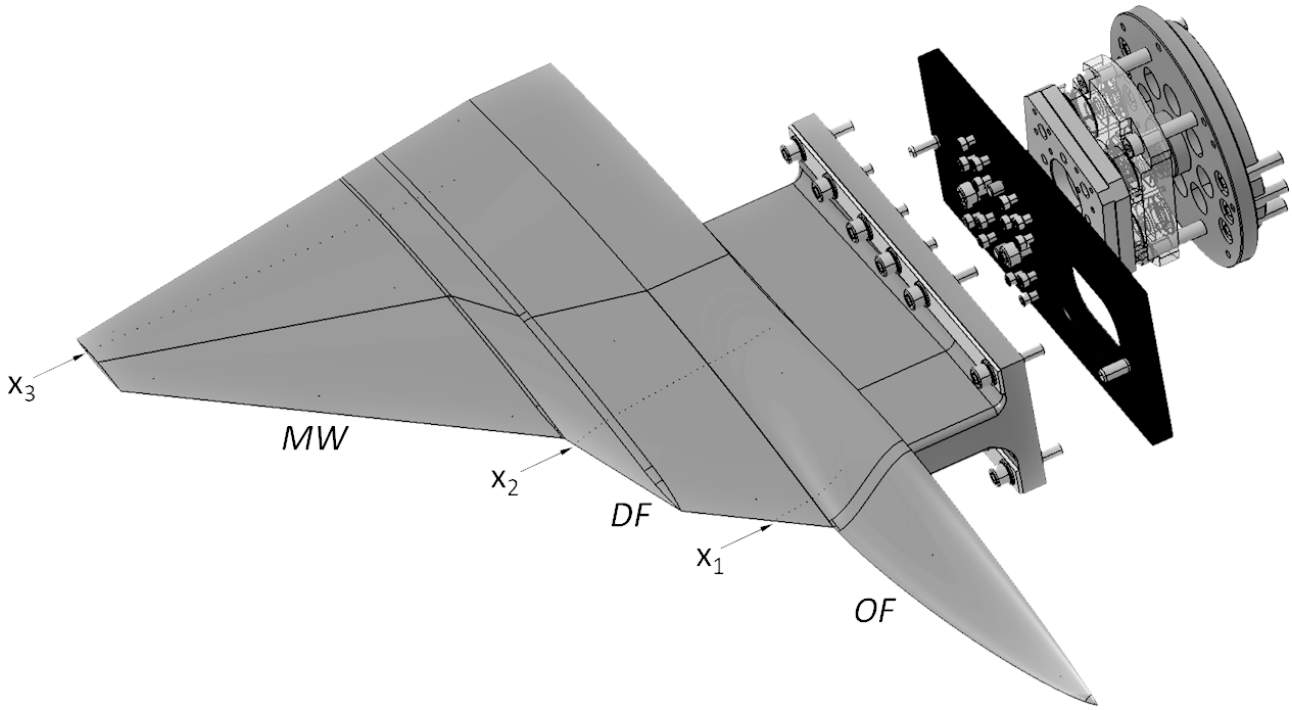

Figure 1 – CAD-model of *DLR-F23* with piezo-electric balance and connecting plates

As a consequence, the vortex system consists of three primary vortices for subsonic flow at the lower swept $45°$ leading edges (MW-, DF- and OF-vortex) and of two vortices for supersonic flow at the higher swept $75°$ leading edges (DF_S- and OF-vortex) [31–36]. The effective Mach-number is basically the Mach-number that acts normal to the leading edge and describes, whether a leading edge is sub- or supersonic and is a function of free stream Mach-number, sweep angle, profile angle and α (see Eq. 1):

$$Ma_{eff} = Ma_{\infty}\sqrt{1-\cos^2(\alpha-\beta')\sin^2\lambda} \tag{1}$$

Additionally, investigations on full-span models need to consider the angle of sideslip as well. Nevertheless, this means a $Ma_{eff} < 1$ enables and a $Ma_{eff} > 1$ suppresses leading edge vortices. From

a fluid dynamical perspective, the Mach-cone aligns more and more with the leading edge for increasing Mach-numbers. As a consequence, the flow around the leading edge diminishes, until no more fluid from the pressure side may flow to the suction side and hence, enable the formation of leading edge vortices. At this point, the leading edge suction subsides as well. Even though, this process is defined by geometrical dependencies, the experiment and CFD show, that utilizable vortex lift capabilities subside earlier at lower Mach-numbers already, than Eq. 1 would suggest. As a result, a combat aircraft design should account for this by pairing the leading sweep angles to a higher Mach-number, in order to guarantee maneuverability by vortical flow throughout the desired flight regime.

2.2 DLR-F23 Sensors

As explained before, the *DLR-F23* semi-span model is dedicated to the research on time-resovled aerodynamics of multi-vortex systems in general, and furthermore to research on these multi-vortex systems behavior under periodic pitching motion and in pitch maneuvers. In order to realize these research goals, the *DLR-F23* is instrumented with 75 unsteady pressure transducers (up to $30kHz$), 4 acceleration sensors and is connected to a piezo-electric six component balance (up to $10kN$ lift, $1kNm$ pitch). With regards to the unsteady pressure transducers, there are three rows (see Fig. 1):

- $x_1 = 320mm$, 12 sensors, y-spacing of $5mm$
- $x_2 = 480mm$, 33 sensors, y-spacing of $5mm$
- $x_3 = 780mm$, 30 sensors, y-spacing of $10mm$

In addition to that, numerous steady pressure transducers (up to $200Hz$) supply boundary conditions at the wind tunnel walls. All collected data is synchronized and sampled with rates between $525Hz$ and $29.2kHz$, or measured for $300s$ and $5.6s$, respectively. In addition to the previously mentioned sensors, an image-based time-resolved pressure-sensitive paint (iPSP) measurement system was installed, which is employed at a sampling rate of $3,2kHz$ [37, 38]. Some iPSP results are subject later on in this work.

2.3 Experimental Set-up

All experiments with the *DLR-F23* are planned for the *Transonic Wind Tunnel Göttingen* of *DNW* and utilize the perforated test section, which operates in-between a Mach-number range of 0.5 to 1.2. Usually, a blockage over 10% is undesirable and the cross-section of the perforated wall set-up measures $1x1m$. Since the model covers a projected area of $0.185m^2$, the limit for the maximum α is at $32.77°$. This area includes the peniche, which fills the stand-off between the model and the wall (see Fig. 2). Regarding the design of the peniche, it has the same trailing edge curvature as the preceding wind tunnel model of the former project *Mephisto* [39]. In addition to that, the peniche's leading edge shares the DF_S-sweep angle of $75°$. The peniche's width of $30mm$ is chosen as such, that it lies within $\delta_{40}...\delta_{60}$ of the boundary layer height δ_{99}. Respectively, this equals a Mach-number inside the boundary layer of $Ma_\delta \leq 0.84...0.90 \cdot Ma_\infty$ [40].
Besides the wind tunnel model and the wind tunnel itself, the hydraulic pitch actuator is an important element of the experiments as well. It allows to hold discrete α, to sweep through a polar at various speeds, to sweep through a wide frequency range while conducting pitch oscillations, or to run small and large amplitude pitch maneuvers and more. Basically, any pitching motion may be programmed into the hydraulic control system, if the motion does not exceed the structural integrity of the model and its sensors. As seen in Fig. 2, a turning disc bridges the connection through the wind tunnel wall between the *DLR-F23* and the hydraulik actuator. Even though the model and the disc sit flush, there is a $0.5mm$ gap between the front and rear of the model and the walls, because the model exceeds the turnings disc's diameter. Special attention had to be paid to the position of the rotational axis. With the aid of CFD-calculations it could be placed as such, that the deviation of the pitching momentum is minimized throughout the test regime, which yields a location of $x = 515mm$ from the model's nose tip. This position is just slightly down-stream of the kink between *MW* and *DF*.

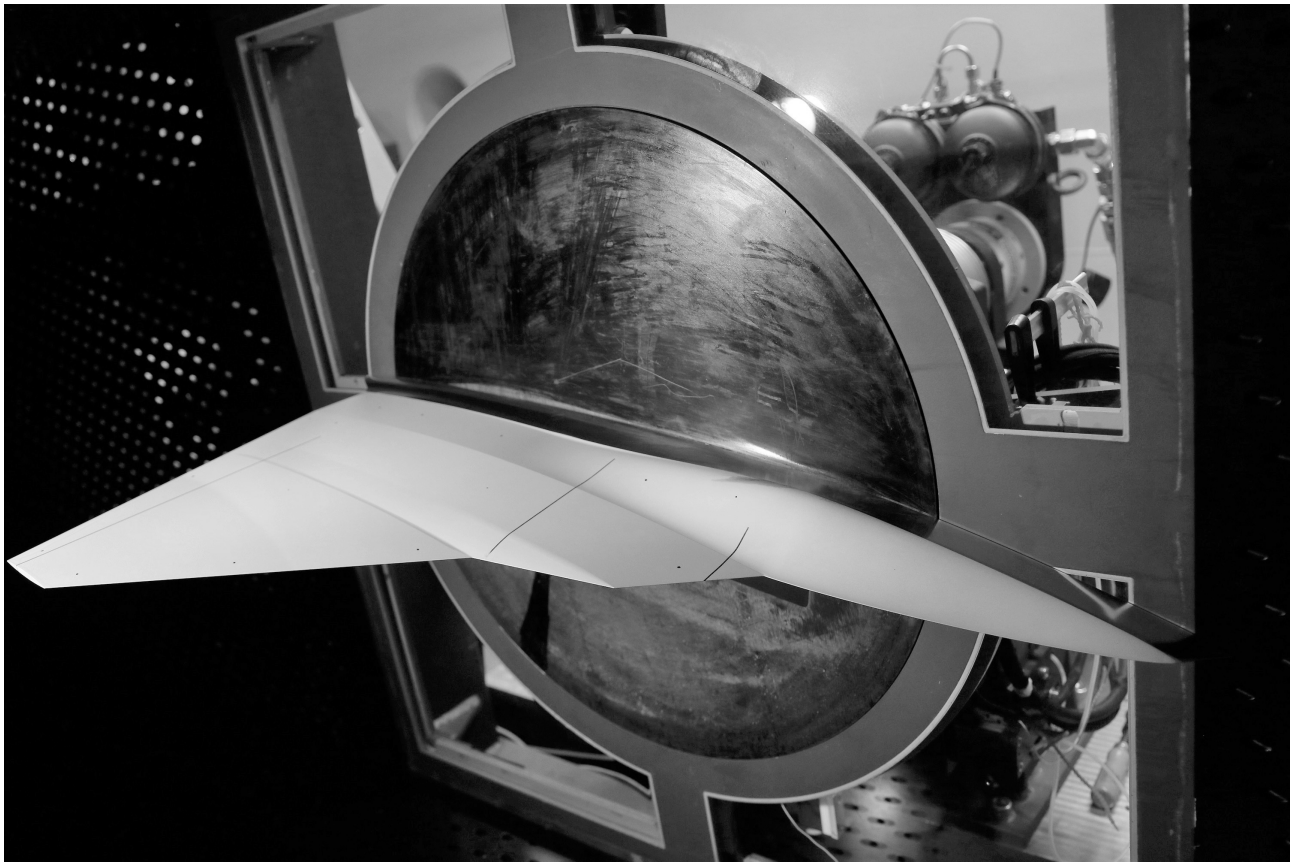

Figure 2 – *DLR-F23* painted for iPSP

2.4 Scope of Measurements

All measurements are taken at a pressure level of $60kPa$ and utilize the maximum Mach-number range of the perforated test section (0.5 to 1.2). If we consider the mean aerodynamic chord (MAC) of $411mm$, this yields a Reynolds-number range of $2.15...3.29 \cdot 10^6$.
There are four major sets of measurements in the experiments, which are explained in the following. A comprehensive overview of these measurements within the Mach-number and α range is provided in Fig. 3.

2.4.1 Large Amplitude Quasi-Steady Polars

In the beginning, the entire Mach-number- and α-envelope is analyzed by conducting continuous pitch sweeps at a rate of $0.1°/sec$ for constant Mach-numbers (see Tab. 1). In particular, the Mach-number increments are $\Delta 0.025$ in-between $0.50...1.00$ and $\Delta 0.050$ in-between $1.00...1.20$. Concerning α, the pitching motion covers $0°...30°$ up to Mach-number 0.9, furthermore covers $0°...25°$ between Mach-numbers $0.925...1.00$, and for the supersonic Mach-numbers $1.05...1.20$ covers $0°...20°$. As a consequence, the time of the quasi-steady pitching motion is $300s$, $250s$ and $200s$. With regards to the resolution, a sampling rate of $F_s = 524.8Hz$ is applied (see also Fig. 3: grey-coloured bars).

large amplitude quasi-stady polars		
Mach-numbers	Δ-Mach-number	α_{max} [°]
0.5...0.9	0.025	30
0.925...1.00	0.025	25
1.05...1.20	0.050	20

Table 1 – Mach-numbers, Mach-numbers increments and maximum α

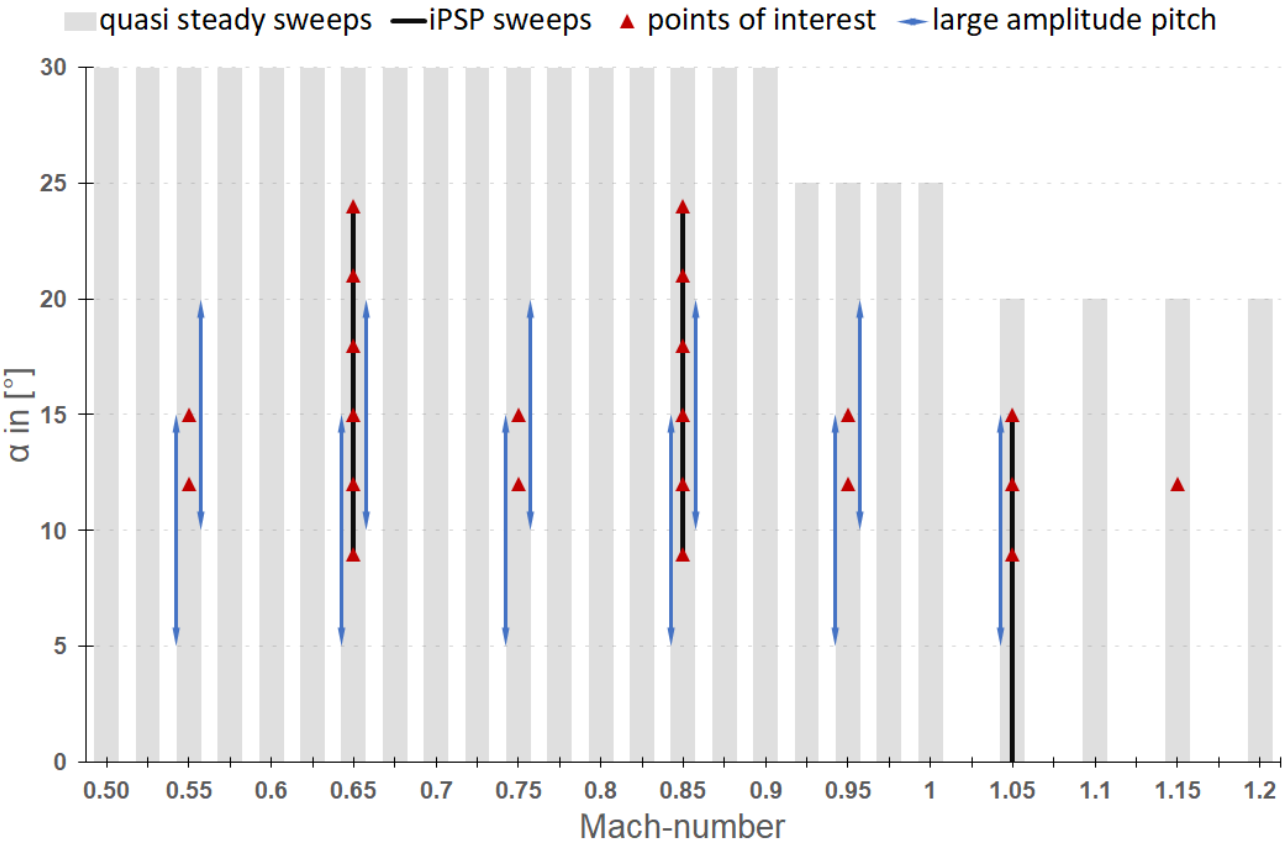

Figure 3 – Overview *DLR-F23* first experiment Mach-number- and α-range
blue lines: shifted left or right for better visability, but meant to belong to Mach-number with ticks, e.g. at exactly 0.55

2.4.2 Points of Interest

Whereas, the quasi-steady polars provide a well resolved overview of global forces and moments, the low sampling rate F_s of these measurements does not allow insights into medium or high fidelity phenomena, and thereby not a thorough analysis in the frequency domain. Thus, the experiments also focus on some selected "points of interest", which are distributed throughout the Mach-number- and α-space in such a way, that the main vortical flow phenomena can be characterized. In total, there are 22 points of interest (see Tab. 2).

Mach-number	α_0	Mach-number	α_0	Mach-number	α_0	Mach-number	α_0
0.50	12	0.65	21	0.85	15	1.05	9
0.50	15	0.65	24	0.85	18	1.05	12
0.65	9	0.75	12	0.85	21	1.05	15
0.65	12	0.75	15	0.85	24	1.15	12
0.65	15	0.85	9	0.95	12	-	-
0.65	18	0.85	12	0.95	15	-	-

Table 2 – 22 points of interest distributed throughout Mach-numbers and α_0

Each of these 22 points is investigated on by four different types of measurements (see Fig. 3: red triangles). At first, the hydraulic system holds the model steady and the sampling rate of the measurement is set to $F_s = 25.6kHz$, which enables an analysis of high fidelity flow phenomena in the frequency domain.
In a second step, the model is pitched slowly through the current point of interest at two different speeds, once in an upward and once in a downward motion for each speed (see Tab. 3). These data sets aid twofold: On the one hand, these small amplitude quasi-steady motions show the existence of

hysteresis effects. Also, the impact of the motion speed is shown, and future wind tunnel experiments can possibly employ a faster pitching speed, which saves time and increases the sampling rate F_s. On the other hand, numerical validations and extensions benefit from these data-sets as well. In case of small deviations in the effective-α between the experimental and numerical domain, the CFD-results and the measured data can be fitted accordingly to a slightly lower or higher α, than was chosen for the simulation.
After these small amplitude quasi steady pitching motions, the wind tunnel model is swept through a frequency range of $0...40Hz$ for three different amplitudes $\Delta\alpha$. As a result, aerodynamic phenomena with eigenfrequencies within that actuated frequency range, or higher harmonics of this frequency range are triggered or experience an excitation. This leads to local and/or global flow stabilization or destabilization. In parallel, the tendency for an excitation of structural modes, or the ability of coupling with structural modes is inspected as well.
At last, an aerodynamic impulse is simulated by fast pitch up and pitch down ramps at two different speeds. Through the introduction of rapid impulses into the aerodynamic system, aerodynamic eigenfrequencies are detected. In addition to that, transfer functions between all sensors may be derived. Last but not least, the inherent stability of the aerodynamic topology is characterized and shows the probability of aerodynamic mode oscillations. A further benefit of these rapid maneuvers is their short duration, which enables a reproduction of these maneuvers in CFD.

procedure	α_0 [°]	$\Delta\alpha$ [°]	[°/s]	t_{msr} [s]	F_s [kHz]
$steady$	α_0	0	0	6.4	25.6
$up_{.01}$	$\alpha_0 - 1$	$+2$	0.01	200	0.78
$down_{.01}$	$\alpha_0 + 1$	-2	0.01	200	0.78
$up_{.1}$	$\alpha_0 - 1$	$+2$	0.1	20	5.47
$down_{.1}$	$\alpha_0 + 1$	-2	0.1	20	5.47
$F_{sweep,.10}$	α_0	± 0.10	0...8	300	0.53
$F_{sweep,.25}$	α_0	± 0.25	0...20	300	0.53
$F_{sweep,.50}$	α_0	± 0.50	0...40	300	0.53
$ramp_{up,20}$	α_0	$+1$	20	6.4	25.6
$ramp_{down,20}$	α_0	-1	20	6.4	25.6
$ramp_{up,40}$	α_0	$+1$	40	6.4	25.6
$ramp_{down,40}$	α_0	-1	40	6.4	25.6

Table 3 – four measurement procedure applied to all 22 points of interest

2.4.3 Time-resolved Pressure Sensitive Paint - iPSP

Next to the 75 unsteady pressure transducers, iPSP is employed at $3.2kHz$, in order to supply surface-covering time-resolved pressure information on the suction-side [37,38]. In total, 25 data sets of iPSP are available, of which 22 are the same, as the points of interest. However, three measurements comprised a quasi-steady sweep at different Mach-number and α combinations (see Tab. 4 and see Fig. 3: black vertical lines).

Mach-number	α_0 [°]	$\Delta\alpha$ [°]	[°/s]	t_{msr} [s]	F_s [kHz]
0.65	9	$+15$	0.1	150	1.024
0.85	9	$+15$	0.1	150	1.024
1.05	0	$+15$	0.1	150	1.024

Table 4 – iPSP quasi-steady sweeps

As mentioned before, all sensor data including the iPSP-data are synchronized in time. Hence, the magnitude of the iPSP is calibrated to the unsteady pressure transducers. It has to be noted, that some surface areas on the wind tunnel model are masked off, for the evaluation of the iPSP-data (see Fig. 4). These locations are the unsteady pressure transducers, also 12 geometrical markers for the

optical calibration of the iPSP-system, a reflecting convex area around the position $(x = 0.3m, y = 0.0m)$ and last but not least at parts of the outer edges.

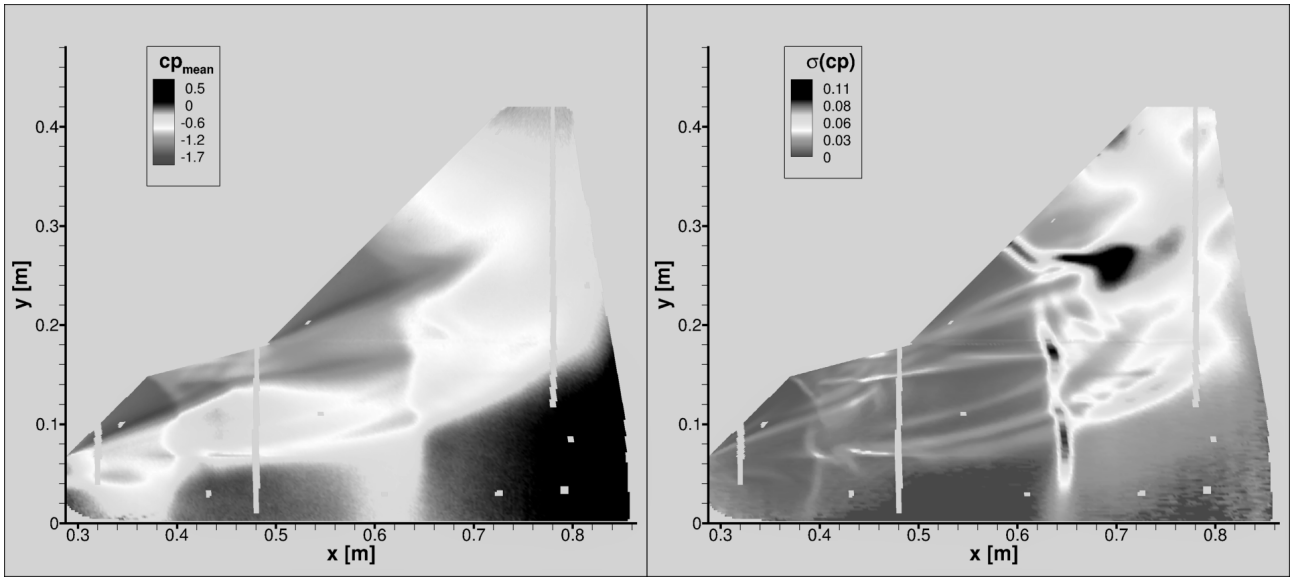

Figure 4 – iPSP on *DLR-F23* Mach-number at 0.85 and $\alpha = 15^\circ$ with masked-off areas

As a result of the iPSP-measurements, information on mean and standard deviation of surface pressure reveal the force and momentum driving topological features as well as their measure of unsteadiness. This data is a valuable reference for qualitative CFD-validation. However, the most precious aspect of iPSP is the evaluation of the entire time-series of instantaneous surface pressures for each individual data-set. In particular time-series analysis of iPSP yields both: transfer functions between local flow phenomena and their impact on the global flow stability, as well as quantitative high fidelity CFD-validation and thus experimental data extension.

2.4.4 Large Amplitude Pitching Maneuvers

In the end of the first experimental campaign with the *DLR-F23* the most structural demanding measurements were conducted. Large amplitude rapid pitching motions show the dynamic gradients of the aerodynamic forces and moments. The motion consists of acceleration, uniform pitch and deceleration, which yields information on aerodynamic inertia, agility performance, and hysteresis effects, such as force overshoots and recovery phases.
As seen in Tab. 5, the pitching direction is either $\Delta 10^\circ$ up or $\Delta 10^\circ$ down for four different α_0. The maneuvers have three different speeds or respectively, last three different periods. With regards to the Mach-numbers, six were investigated on $(0.55; 0.65; 0.75; 0.85; 0.95; 1.05)$, of which the last one at 1.05 was left out for the up_{10}- and $down_{20}$-maneuvers (see Fig. 3: blue lines with arrows).

maneuver	α_0 $[^\circ]$	$\Delta\alpha$ $[^\circ]$	$[^\circ/s]$	t_{mnv} $[ms]$
up_5	5	$+10$	$20, 40, 60$	$500, 250, 166$
$down_{15}$	15	-10	$20, 40, 60$	$500, 250, 166$
up_{10}	10	$+10$	$20, 40, 60$	$500, 250, 166$
$down_{20}$	20	-10	$20, 40, 60$	$500, 250, 166$

Table 5 – large amplitude pitching maneuver test matrix

In the same manner as the $\Delta \pm 1^\circ$ ramps within the points of interest investigations, a CFD-calculation for these large amplitude maneuvers is a feasible option. Eventually, the identification of the vortex dynamics throughout these maneuvers reveals locations as well as time-scales of stabilizing or destabilizing topological features, which likely differ from stationary and small amplitude measurements.
All in all, the presented measurements set-up a profound research data-base, that will be extended further in the second wind tunnel campaign.

3. Numerical Set-up

The numerical calculations aim to prove the capabilities of the TAU-code to reproduce the flow phenomena, as they were observed in the *DLR-F23* wind tunnel experiments. As an outcome, the CFD results enable a analysis of the flow field in space and time and thus yield further causalities between flow topology features and flow instabilities, than may be derived from experimental data. A rather demanding test case from the experiments points of interest is chosen, in order to demonstrate the numerical ability to reproduce the unsteady flow topologies. This test case is at Mach-number 0.85 and $\alpha = 21°$.

3.1 Grid Design

Instead of modeling the wind tunnel test section or parts of it, this numerical set-up consists of the wind tunnel model, a symmetry plane and a hemispheric farfield. The wind tunnel models surface is discretized by triangles and wrapped by 33 prism layers. All other elements are tetrahedrons or pyramids, whereas the latter are negligible in number. In order to save grid points and thereby computing time, the TAU-code solution-based mesh refinement is used to adapt an initial coarse grid to the flow. Tab. 6 provides a rough overview of the initial and the refined grid.

feature	edge length [mm]	rel. to MAC	total N°	refined [mm]	refined rel.	total N°
farfield	10^8	$243 \cdot 10^3$	-	-	-	-
surf. triangles	2	$4.9 \cdot 10^{-3}$	$0.9 \cdot 10^6$	1	$2.4 \cdot 10^{-3}$	$2 \cdot 10^6$
prisms	2	$4.9 \cdot 10^{-3}$	$27 \cdot 10^6$	1	$2.4 \cdot 10^{-3}$	$65 \cdot 10^6$
tetrahedrons	8	$19.5 \cdot 10^{-3}$	$13 \cdot 10^6$	2	$4.9 \cdot 10^{-3}$	$99 \cdot 10^6$
pyramids	-	-	$23 \cdot 10^3$	-	-	$23 \cdot 10^3$
points	-	-	$16 \cdot 10^6$	-	-	$50 \cdot 10^6$

Table 6 – initial and refined numerical grid: length scales and number of elements

3.2 Solution-Based Adaptation

When solution-based adaptation is applied to unsteady flow cases, a statistically converged solution is needed. This solution contains mean values ($\overline{\phi}$), and standard deviations ($\sigma(\phi)$) or fluctuations (ϕ') of the primitive variables. If the solution is not statistically converged, yet or if instantaneous values of the primitive variables are used for the adaptation, chances are that the refined areas do not cover all relevant flow features. As a consequence, the grid could then force the flow into the refined mesh areas and hence, introduce an relevant systematic error.

For the presented case, an difference indicator is employed, that analyses the solution of the coarse grid with regards to local differences in the mean pressure coefficient ($\overline{cp}$), the standard deviation of pressure ($\sigma(p)$) and the mean turbulent viscosity ($\overline{\mu^t}$). As an outcome of this analysis, all edges of all elements in the numerical grid are ranked. In the current case, the maximum number of grid points is limited to $50 \cdot 10^6$, so only a limited number of element edges are refined. In case multiple edges of an element are marked for refinement, this element is refined isotropically. This process is conducted several times for the same flow field solution, which has two reasons. First, an element can only be touched once per refinement, but the initial tetrahedral edge length is $8mm$ and the desired edge length is $2mm$. Consequently, at least two iterations are needed. Second, the adaptation procedure can refine, but also de-refine edges, once they were refined previously. So, by running the adaptation numerous times, the grid re-balances itself until no major changes are seen.

Furthermore, an user-defined level of refinement should be set for this approach, which is 2 in this case. Thereby, an edge may not be refined more than two times, which corresponds to the desired final tetrahedral edge length of $2mm$. Also, in order to prevent massive surface refinement, the minimum edge length is limited to $1.4mm$. Last but not least, it was chosen to save grid points, by not refining greater parts of the wake. An impression of the simulated flow on a grid, that is adapted by this method, is seen in Fig . Therein the mesh-plane depicts the end of the refined area, whereas the

symmetry is colored in $\overline{cp}$. An outline of the unsteady flow is shown by an instantaneous λ_2-criterion, which is colored by $\overline{\mu^t}$.

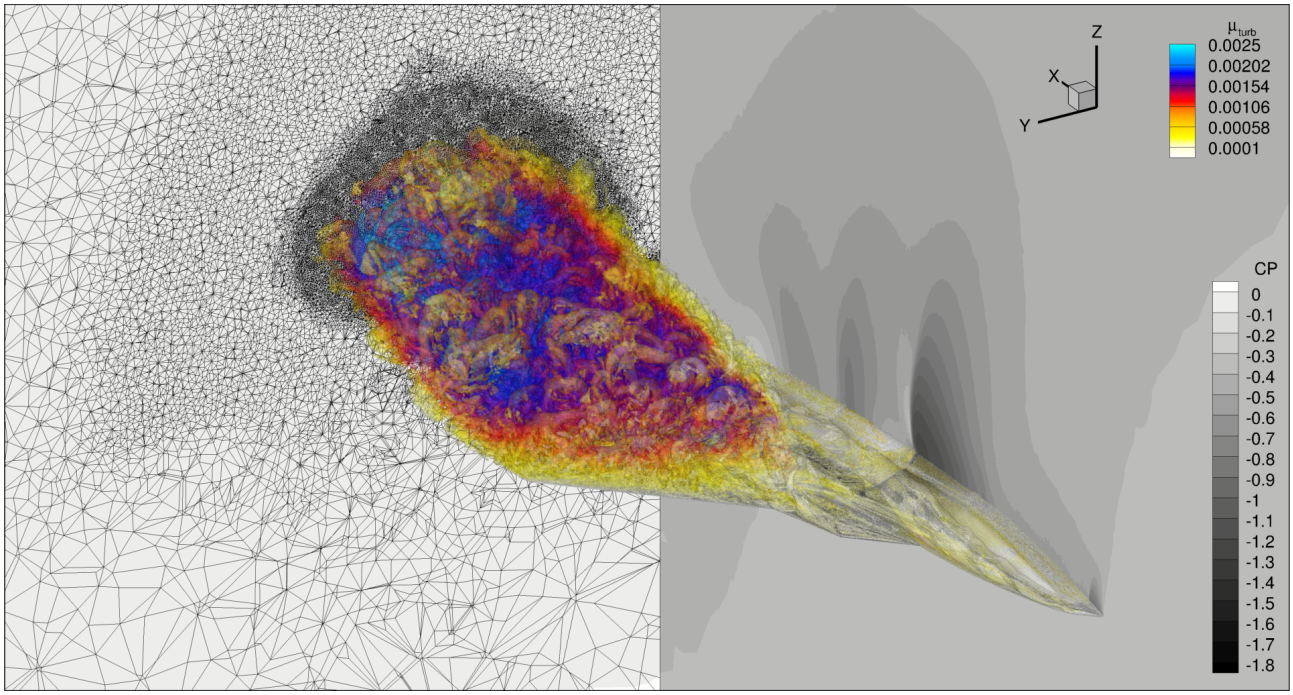

Figure 5 – hybrid-RANS-LES simulation of the *DLR-F23* at Mach-number 0.85 and $\alpha = 21^\circ$ on solution adapted grid

3.3 TAU-code Settings

The presented CFD-calculations use the TAU-codes implicit dual time stepping scheme, which consists of inner iterations (quasi-steady time steps) and outer iterations (physical times steps). The employed central scheme yields second order accuracy in space and in time. With regards to the CFL-number, it may be chosen as high as possible for the inner iterations to accelerate convergence with negligible impact on accuracy. However, this is not applicable to the outer iterations for the current numerical objective. Even though, implicit schemes are stable at high CFL-numbers, accuracy suffers, when the CFL-number of physical time steps is greater than unity. Usually, the CFL-condition is linked to the free stream velocity u_0, however delta wing flows comprise vortex core velocities, which are as high as $3 \cdot u_0$ [7]. In order to account for this, but assuming that the peak core velocities are rather stable than fluctuating, a reference velocity of $2.5 \cdot u_0$ is chosen. Furthermore, the tetrahedral edge length of $l_{tet} = 2mm$ is taken into account, which yields a time step size of:

$$\Delta t = \frac{l_{tet}}{2.5 \cdot u_0} = 2.5 \cdot 10^{-6} s \tag{2}$$

Progress of the outer iterations through time is linked to reaching the convergence criteria of the inner iterations. Cauchy-convergence, that monitors lift, drag and pitching momentum of the inner iterations, is satisfied when the absolute difference of 30 consecutive inner iterations falls below $\Delta 10^{-7}$ for all three monitor values.

With regards to the turbulence modeling, the simulation employs a hybrid-RANS-LES scheme, that blends the one-equation Spalart Allmaras model in its negative formulation (SA-neg) [41] with an improved delayed detached-eddy simulation (IDDES) [42].

4. Results

4.1 Experimental Results

A great amount of time-resolved data is available from the first wind tunnel experiment with the *DLR-F23*, which now needs to be analyzed and investigated on. Some first insights are given in the following sections of this work.

4.1.1 Global Pitching Momentum Characteristics

As a matter of fact, delta-wing based combat aircraft planforms need to meet demanding requirements with regards to the pitching momentum coefficient c_{my}, which frames the possible maneuvers within the desired Mach-number- and α-flight regime*. Basically, the coefficient dictates whether the global aerodynamic momentum pitches the aircraft's nose up ($c_{my} > 0$), or if the nose is pitched down ($c_{my} < 0$).

In particular, there are three major characteristics, which need attention, when evaluating c_{my}. On the one hand, the variance of the c_{my}-amplitude throughout the flight regime is desired to be small, because small amplitudes ask either for small flight control devices, or for small deflections of the flight control devices. Partly in contradiction to that, agility within maneuvers is achieved by high gradients of c_{my}. In order to combine both, small amplitudes and high gradients, the direction of c_{my} must change multiple times throughout a α-sweep. As a third aspect and as a result of the alternating sign of $c_{my}(\alpha)$, a controlled pitching motion has either to overcome a restoring momentum (when the direction of motion and c_{my} are misaligned) or is enforced (when the direction of motion and c_{my} are aligned). Thereby, phases of alignment and misalignment can alter throughout the maneuver.

A representative polar at Mach-number 0.85 in shown in Fig. 6. Both are shown, the mean-c_{my} and the actual raw data as scatter plot. As can be seen, the unsteadiness of the flow increases with α, while $\delta c_{my}/\delta\alpha$ experiences a number of changes in sign.

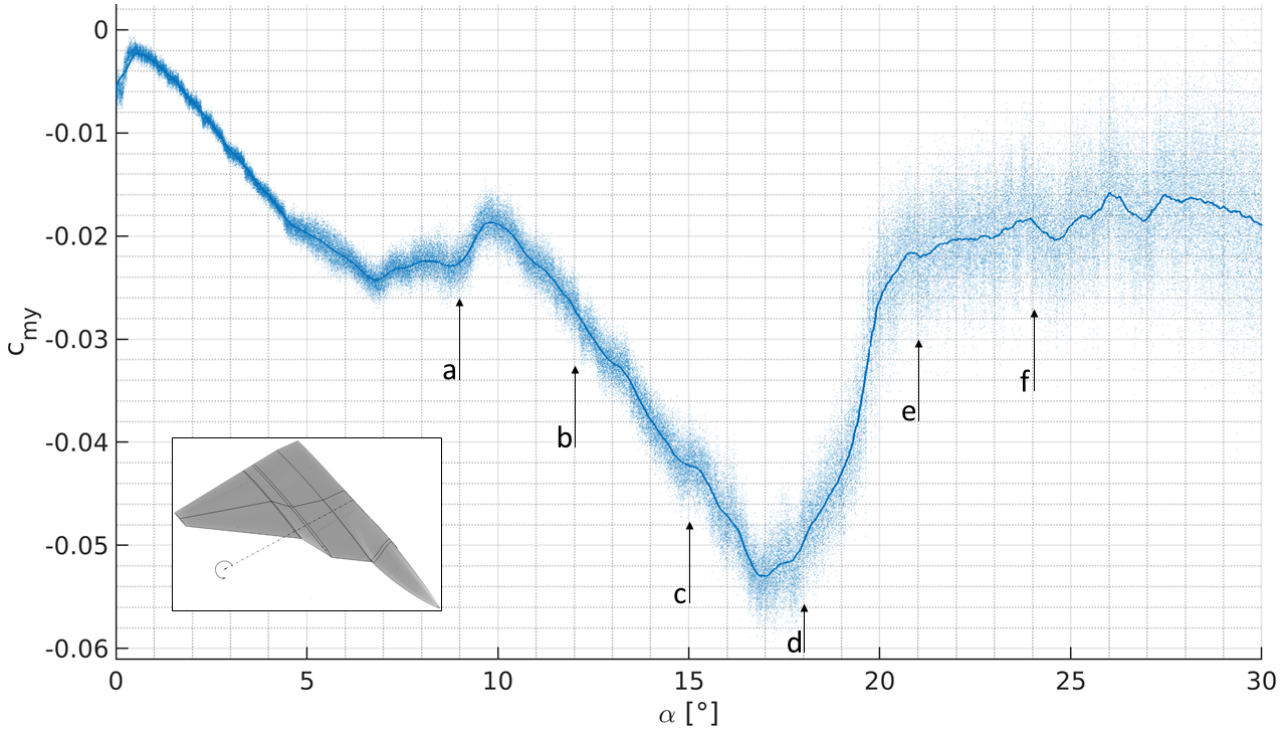

Figure 6 – c_{my} for quasi-steady polar at Mach-number 0.85; iPSP-data for α of a-f in Appendix

4.1.2 Mach-number Effects on Vortex-Intertwining

In the past, research focused on vortex-intertwining effects, but not so much on the reversal of this process. Usually, intertwining is connected to an increase in α, however, there is also a strong Mach-number dependency. An increase in Mach-number reduces the vortex strength and the unsteadiness of the flow. This can be seen throughout Figs. 7, 8 and 9, which show iPSP-results for a constant $\alpha = 15°$ at three different Mach-numbers of 0.50, 0.75, and 0.95.

As a consequence, the vortices decrease in diameter and the intertwining reduces. Eventually, a de-twining process begins, until the vortices are aligned more or less parallel. Thus, the phenomenon of

*Additionally, the influence of yaw and roll maneuvers, which lead to asymmetric Ma_{eff} on the luv and lee side, have to be considered as well. Yet, this work focuses on a semi-span model, so that these characteristics need no further attention herein.

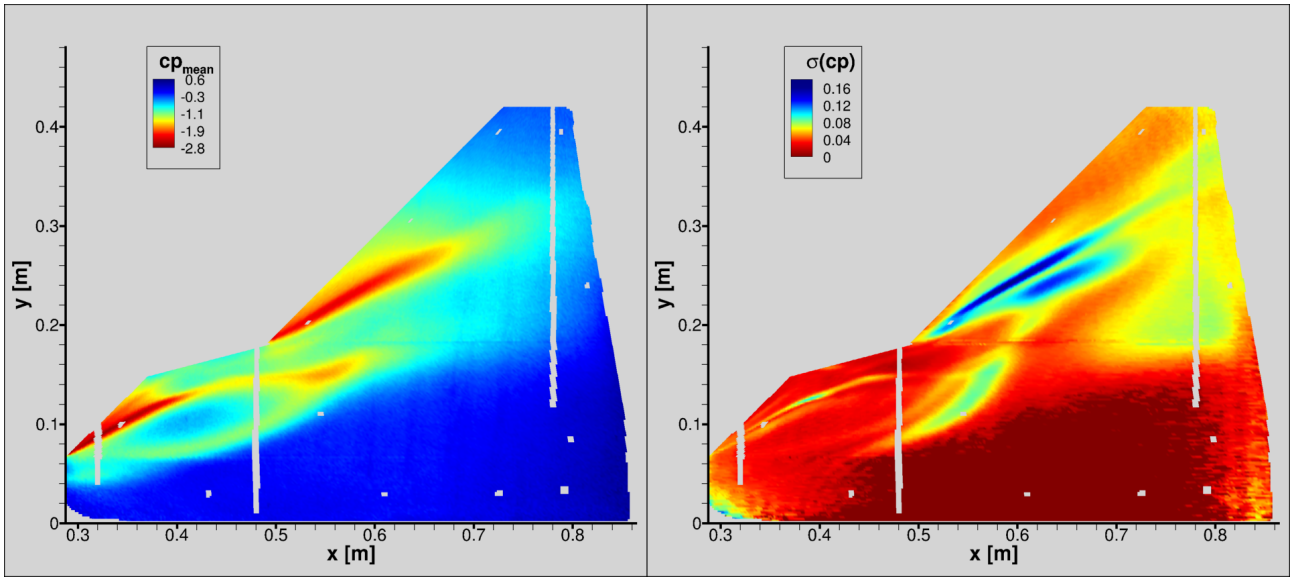

Figure 7 – cp_{mean} and $\sigma(cp)$ at Mach-number 0.55 and $\alpha = 15°$, vortices strongly intertwined

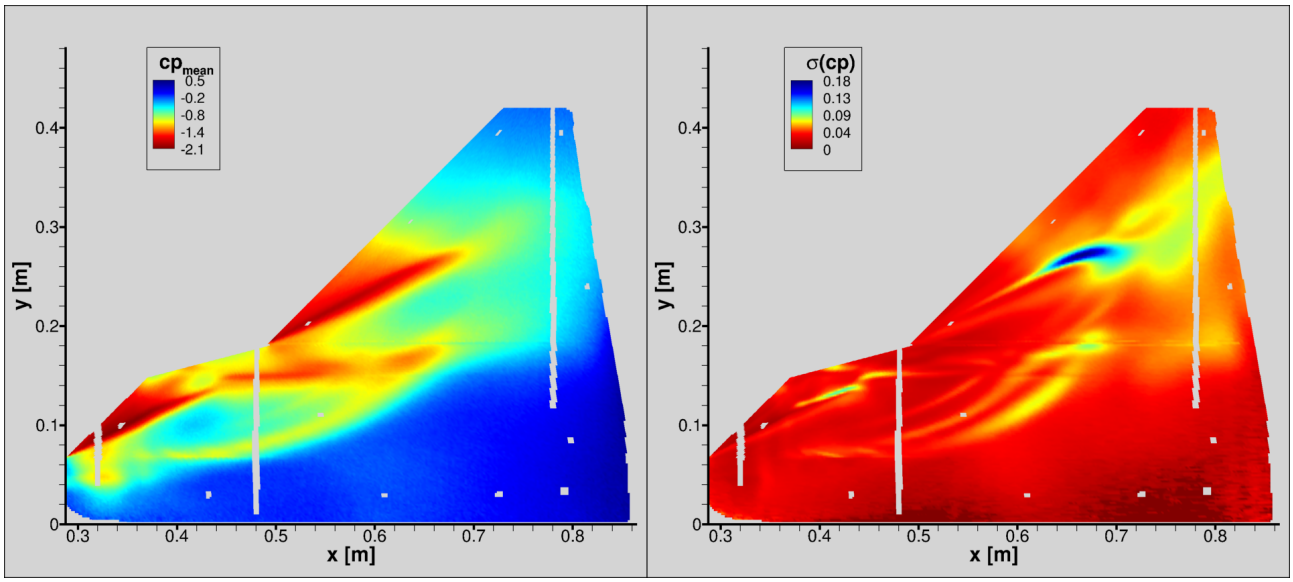

Figure 8 – cp_{mean} and $\sigma(cp)$ at Mach-number 0.75 and $\alpha = 15°$, vortices intertwined further downstream

de-twining can occur, whenever the aircraft accelerates at nearly constant α. A reasonable scenario is e.g. a combat aircraft, that rapidly accelerates out of a narrow turn, in order to transition into cruise quickly. The opposite is true for a deceleration, which would encourage intertwining. A corresponding maneuver would be e.g. a strong deceleration, in order to initiate a narrow turn for fast engagement. In particular, the use of unmanned combat aircraft increases the importance of these Mach-number effects, since the limits for acceleration forces depend on structure only.

4.2 Numerical Results

The experimental data show a highly unsteady vortical flow at Mach-number 0.85 and $\alpha = 21°$, which is a demanding benchmark for the DLR-TAU-code solver. For this flow case, all three leading vortices experience interacting breakdown, whose positions are predicted by CFD close to the experimental iPSP-data. Furthermore, two dominant shocks occur in the experiment, whereas the numerical results show an additional shock near the trailing edge, which is seen in Fig. 5. The first shock forms just before the kink between *MW* and *DF*, but is rather steady in its position. In contrast to this, the second shock is further downstream and is linked to the three oscillating vortex breakdowns.

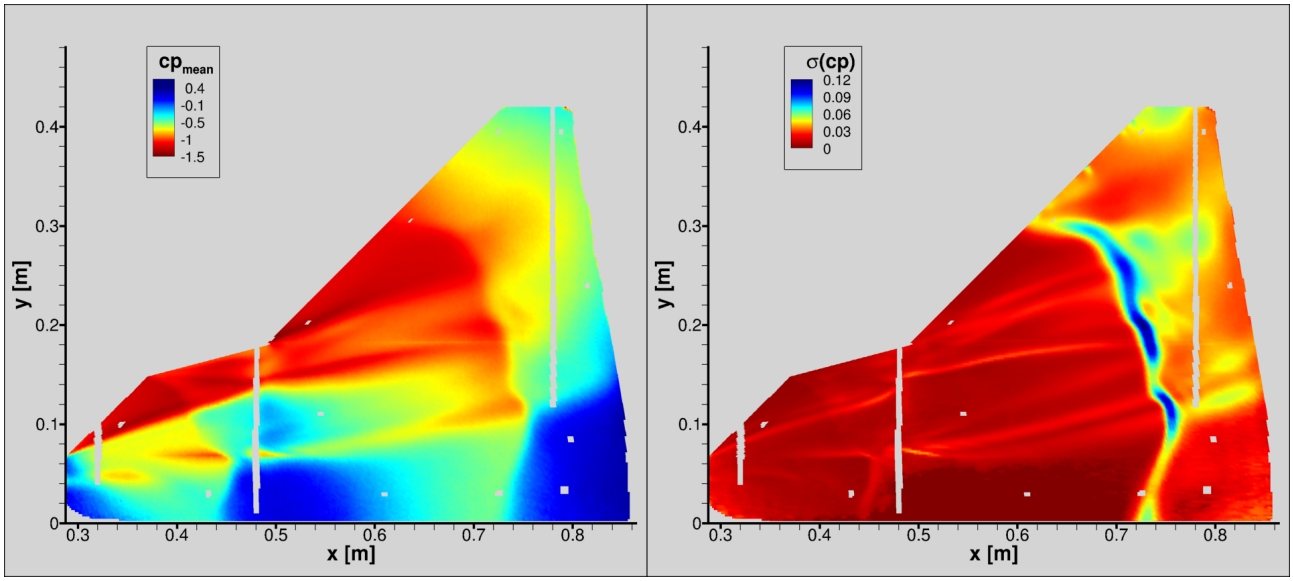

Figure 9 – cp_{mean} and $\sigma(cp)$ at Mach-number 0.95 and $\alpha = 15°$, vortices de-twined

Thereby, this second shock experiences large lateral oscillations.

4.2.1 Comparison of pressure coefficient between CFD and experiment

The numerical simulation proves to resolve the overall flow topologies as seen in the experiments. However, the comparison between the mean pressure coefficients ($\overline{cp}$) of CFD and iPSP show some differences as seen in Fig. 10. These differences are likely a result of two types of missing boundary conditions, which are of geometrical and of aeroelastic kind.

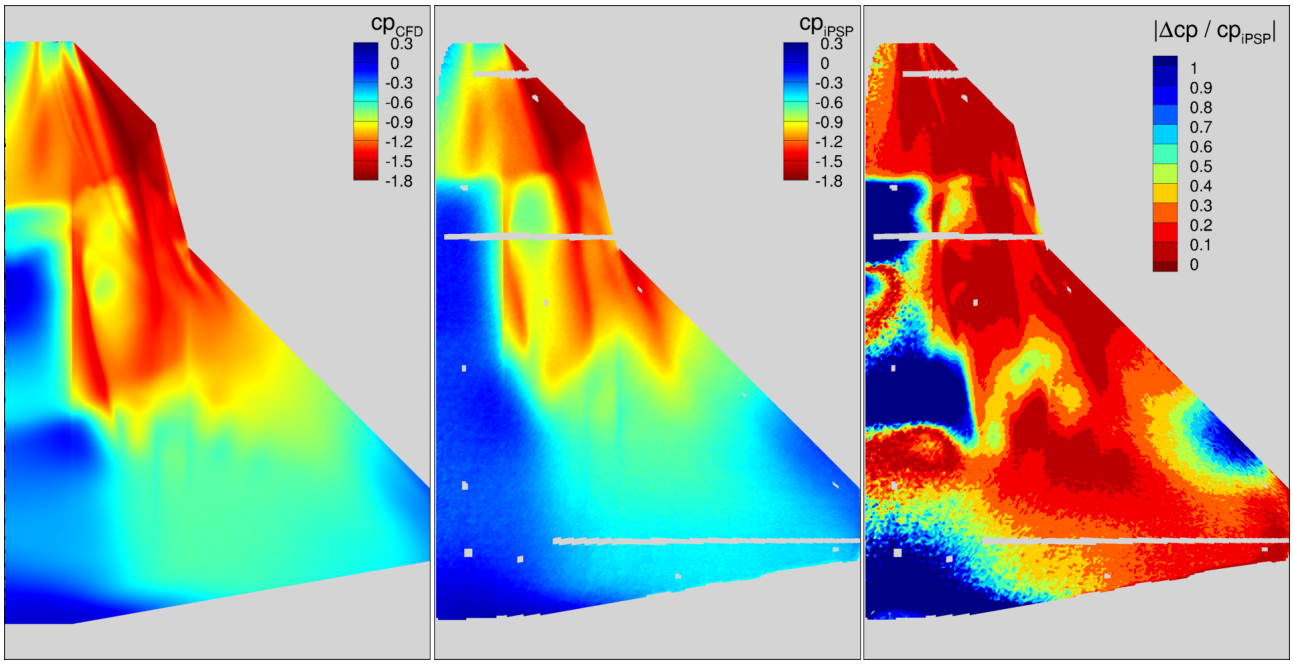

Figure 10 – left: $\overline{cp}$-CFD; mid: $\overline{cp}$-iPSP; right: relative difference

Even though the *DLR-F23* wind tunnel model is made from high grade aluminum and passes the high safety standards of the DNW-TWG, it was also constructed to show a structural response to aerodynamic forces. Hence, the outer portion of the *MW* experiences some degree of torsion and of bending, which is expected at such a Mach-number and angle of incidence. Consequently, the local effective angle of incidence increases, which in this flow state forces the tearing of the feeding sheet upstream. Additionally, structural excitation of the *MW* is expected as well. An indication for those

two assumptions is the high unsteadiness of the surface pressure in this region, which is seen in the iPSP results in Fig. 17 in the Appendix.
With regards to the geometrical boundary conditions, the current numerical set-up features a symmetry plane, instead of a frictional wall. Thus, the inboard position of the shocks differs as well. Besides those systematical errors, the overall topological representation of the mean pressure coefficient is in acceptable agreement.

4.2.2 Occurence toplogical mode instabilites

After evaluating the representation of the mean flow, the question raises whether the unsteady effects of the experiment are found in the simulation as well. In this particular flow case, it can be seen, that the flow topology is not clearly defined, but switches between two unstable states. In the first flow state, the *MW*-vortex is completely burst, while the breakdowns of the *DF*- and *OF*-vortex are at a similar position, also the second dominant shock is attached to all three breakdown positions. With regards to the second flow state, the *MW*-vortex has a breakdown oscillation further downstream, which applies to the other two vortices and the shock as well. This phenomenon can be seen in the standard deviation of the pressure coefficient of the iPSP-data in Fig. 17, which incorporates both flow topologies.
If considered, that all distinct unsteady structures contribute to the global unsteady characteristics of a specific flow state [15], then a vortex dominated flow topology, has its specific topological modes. These modes alternate in time. As a consequence, a PSD-analysis would yield the frequency content of multiple topology modes indistinguishable. Therefore, a CWT-analysis on behalf of the pitching momentum coefficient is performed, in order to analyze the frequencies of the flow over time. A comparison of experimental and numerical data show good agreement of the major modes. As seen in Fig 11, the CWT shows the varying frequencies of the flow over time.

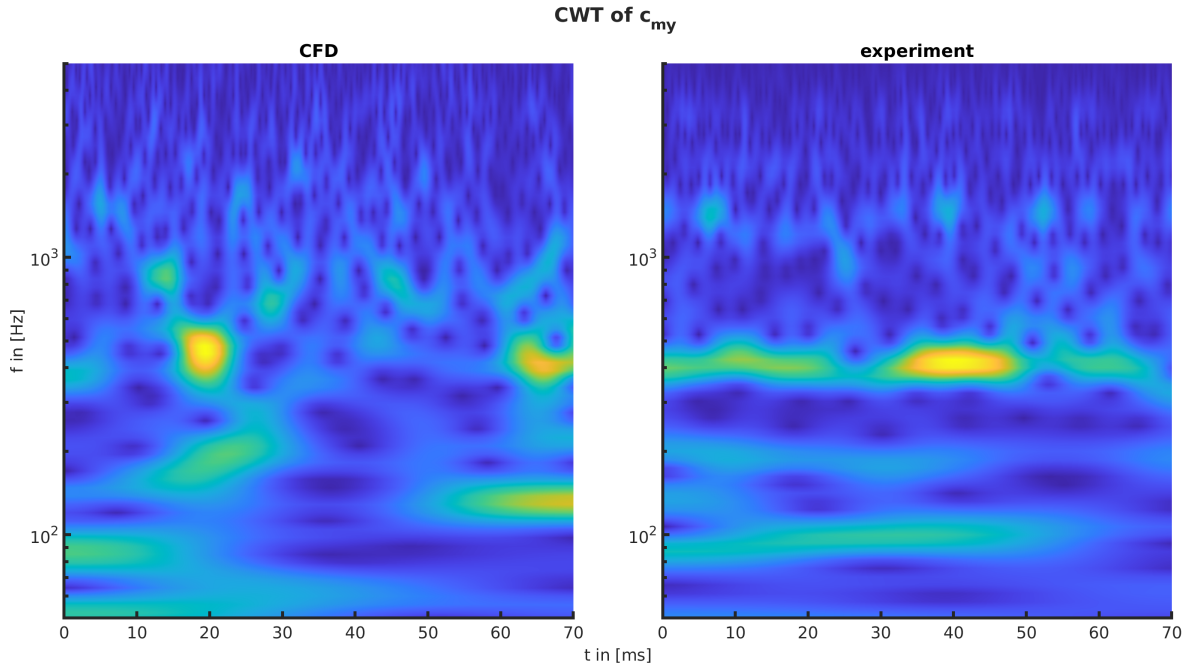

Figure 11 – left: CWT of cm_y in experiment and CFD with mode switch at $\sim 400Hz$

Even though, the experimental data covers $6.4s$ of time, for a better comparability only $70ms$ are shown, which equals the time of the numerical simulation, over which the mean data discussed before was sampled (with regards to the MAC, $70ms$ equal 52 convective time units). Within these $70ms$ two mode alternations occur at $\sim 20ms$ and $\sim 65ms$ in CFD and three mode alternations at $\sim 20ms$, $\sim 49ms$ and $\sim 67ms$ in the experiment. These are not only marked by alternations of the topology mode at $\sim 400Hz$, but also announced by drops and followed by a sudden compensating overshoot in cm_y and furthermore a drop in Mach-number, which is presented in Fig. 12.

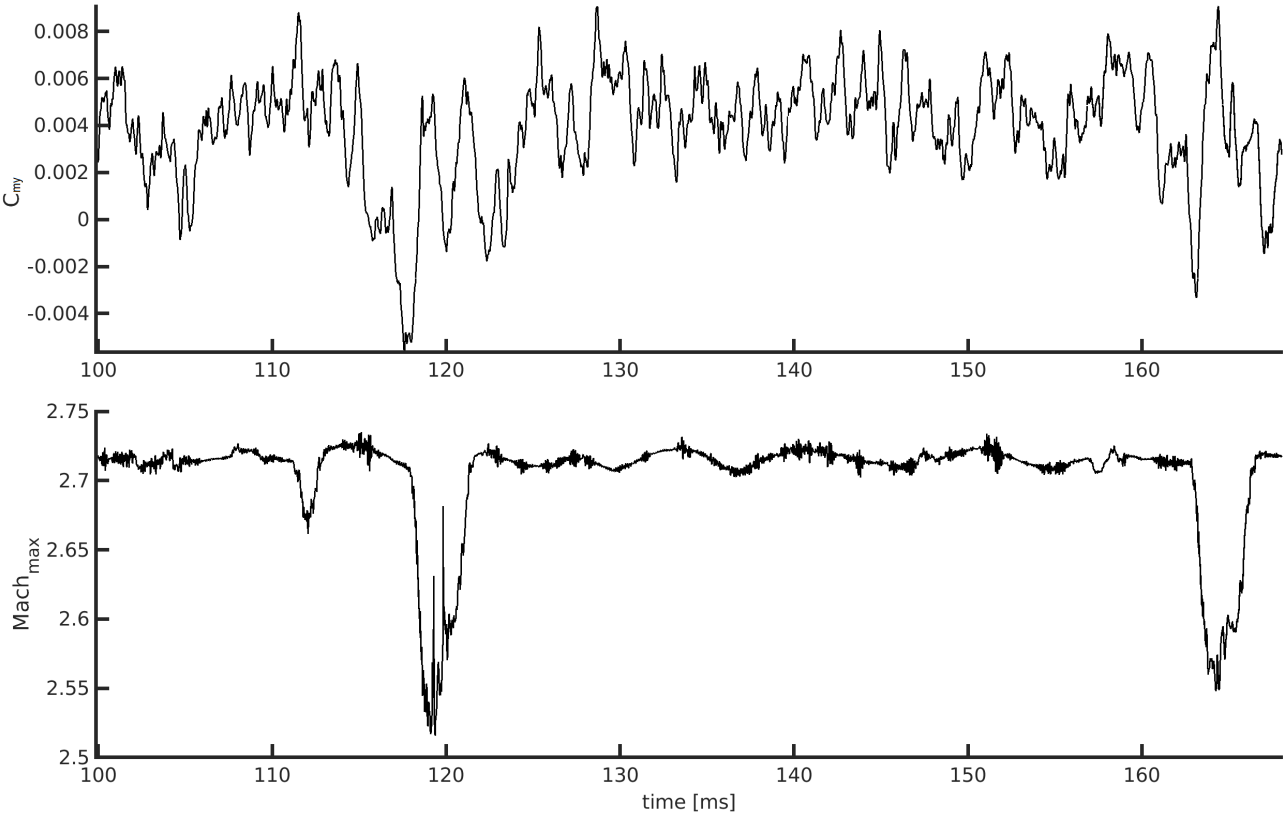

Figure 12 – indication of mode alternation in cm_y and max. Mach-number [CFD from $100ms$ to $170ms$]

However, the data suggest, that the flow in the numerical simulation favors first flow state, whereas the second flow state is dominant in the experiment. This effect could be attributed to the wind tunnel walls, as they limit the radial vortex expansion. Hence, the inclusion of all walls as boundary condition, could be necessary for a complete numerical representation of the experiment. Nevertheless, the underlying mechanism of this flow instability occurs in the current CFD-set-up, which enables more profound analysis of this phenomenon in the future.

5. Conclusion & Outlook

After completing the first wind tunnel campaign with the *DLR-F23*, a detailed data base is available, which will contribute to progress in research on vortical flow over delta wings. The Mach-number- and α-regime is scanned by pitching in a quasi-steady motion through the polars first, then 22 points of interest are investigated on with several measurement procedures. Additionally, time-resolved pressure sensitive paint is employed on these 22 points, as well as on three quasi-steady pitching motions. Furthermore, large amplitude rapid pitch maneuvers are conducted for various speed-, α- and Mach-number combinations.

Some first insights from the data reveal how the topological evolution of the vortex system impacts the global pitching momentum characteristics. Also, vortex de-twining and flow topology mode alternations are discussed and are subject of further investigations. With regards to the numerical set-up, the comparison to the experimental data suggests, that the hybrid-RANS-LES approach is capable to reproduce even very demanding flow cases. In particular, unsteady phenomena are well resolved. However, for an more accurate replication of the experimental data, the boundary conditions need to be refined further.

In order to extend the research on the vortex flow of the *DLR-F23* in particular, and to increase the knowledge on the general mechanisms of flow instabilities and flow evolution, some of the current and planned work is as follows:

- in-depth data analysis in the frequency domain and with a focus on transfer functions, correlations and recurrence of unsteady phenomena (POD, CWT, etc.)

- enhanced flow topology assessment by implementation of new analytical analysis [43]
- system identification of the *DLR-F23* and CFD-FEM-coupled calculations to reproduce structural deformation and excitation [44, 45]
- extended boundary conditions with viscous walls at model inboard side and inviscid walls for the remaining three walls
- also, wind tunnel experiment digitalized by laser scan, to enable CFD-calculations with even more exact geometrical boundary conditions
- 2nd wind tunnel test campaign with time-resolved PIV, to supply field data and length scale information
- preparation of next project with full-span model in a low-speed closed loop set-up, controlled by leading edge slats and pneumatic actuators

Acknowledgments

The authors thank the team Aeroelastic Wind Tunnel Experiments of the DLR Institute of Aeroelasticity, in particular Mr. J. Nuhn, Mr. T. Büte and Mr. H. Ernst, and the team of Experimental Methods of the DLR Institute of Aerodynamics and Flow Technology. Furthermore, the authors thank the DLR Engineering Departement (SHT) and the DNW-TWG.
The authors gratefully acknowledge that this work could be conducted within the DLR project *Diabolo*, which is funded by the German Ministry of Defence and the Federal Office of Bundeswehr Equipment, Information Technology and In-Service Support (BAAINBw). The project *Diabolo* is dedicated to the exploration of technologies and design methodologies, that are relevant for the development of next generation combat aircraft.

Copyright Statement

The authors confirm that the DLR, holds copyright on all of the original material included in this paper. The authors also confirm that they have obtained permission, from the copyright holder of any third party material included in this paper, to publish it as part of their paper. The authors confirm that they give permission, or have obtained permission from the copyright holder of this paper, for the publication and distribution of this paper as part of the ICAS proceedings or as individual off-prints from the proceedings.

References

[1] E. C. Polhamus, “Predictions of vortex-lift characteristics by a leading-edge suctionanalogy,” *Journal of Aircraft*, 1971.
[2] D. S. Miller and R. M. Wood, “Leeside flows over delta wings at supersonic speeds,” *Journal of Aircraft*, 1985.
[3] D. Rockwell, “Three-dimensional flow structure on delta wings at high angle-of-attack-experimental concepts and issues,” in *31st AIAA Aerospace Sciences Meeting*, 1993.
[4] R. C. Nelson and A. Pelletier, “The unsteady aerodynamics of slender wings and aircraft undergoing large amplitude maneuvers,” *Progress in Aerospace Sciences*, 2003.
[5] J. M. Luckring, “A survey of factors affecting blunt leading-edge separation for swept and semi-slender wings,” *28th Applied Aerodynamics Conference AIAA*, 2010.
[6] M. G. Hall, “Vortex breakdown,” *Annual Review of Fluid Mechanics*, 1972.
[7] F. M. Payne, T. T. Ng, R. C. Nelson, and L. B. Schiff, “Visualization and wake surveys of vortical flow over a delta wing,” *AIAA*, 1988.
[8] O. Lucca-Negro and T. O’doherty, “Vortex breakdown: a review,” *Progress in Energy andCombustion Science*, 2001.
[9] D. Hummel and G. Redeker, “A new vortex flow experiment for computer code validation,” in *RTO AVT Symposium*, 2003.
[10] S. Z. Pirzadeh, “Vortical flow prediction using an adaptive unstructured grid method,” tech. rep., NASA, 2003.

[11] A. Schütte, G. Einarsson, A. Madrane, and B. Schoening, "Numerical simulation of manoeuvring aircraft by aerodynamic and flight-mechanic coupling," tech. rep., DLR, 2003.

[12] I. Gursul, M. R. Allan, and K. J. Badcock, "Opportunities for the integrated use of measurements and computations for the understanding of delta wing aerodynamics," *Aerospace Science and Technology*, 2005.

[13] S. A. Morton and D. R. McDaniel, "F-16xl simulations at flight conditions using hybrid near-body/offbody computational fluid dynamics," *Journal of Aircraft*, 2017.

[14] J. M. Luckring, "The discovery and prediction of vortex flow aerodynamics," *The Aeronautical Journal*, 2019.

[15] L. Schiavetta, K. Badcock, and R. Cummings, "Comparison of des and urans for unsteady vortical flows over delta wings," in *45th AIAA Aerospace Sciences Meeting and Exhibit*, 2007.

[16] R. M. Cummings, S. A. Morton, and D. R. McDaniel, "Experiences in accurately predicting time-dependent flows," *Progress in Aerospace Sciences*, 2008.

[17] M. Rein, "Subsonic, transonic and supersonic wind tunnel tests of the generic slender wing configuration dlr-f22 with leading-edge vortex controllers and strakes," *DLR report*, 2022.

[18] J. Zastrow, "Characterizing a multi delta wing for aeroelastic wind tunnnel experiments," *IFASD*, 2019.

[19] J. Zastrow, "Fast preliminary fluid mechanical analysis of fighter aircraft wind tunnel models by application of grid adaptation techniques," *NATO-AVT-324 - Multi-Disciplinary Design Approaches and Performance Assessment of Future Combat Aircraft*, 2020.

[20] G. Erickson and J. Brandon, "On the nonlinear aerodynamic and stability characteristics of a generic chine-forebody slender-wing fighter configuration," in *5th Applied Aerodynamics Conference*, 1987.

[21] S. B. Kern, "Vortex flow control using fillets on a double-delta wing," *Journal of Aircraft*, 1993.

[22] R. C. Grismer, D. S.; Nelson, "Double-delta-wing aerodynamics for pitching motions with and without sideslip," *Journal of Aircraft*, 1995.

[23] N. G. Verhaagen, L. N. Jenkins, S. B. Kern, and A. E. Washburn, "A study of the vortex flow over 76/40-deg double-delta wing," tech. rep., NASA, 1995.

[24] S. K. Hebbar, M. F. Platzer, and W. H. Chang, "Control of high-incidence vortical flow on double-delta wings undergoing sideslip," *Journal of Aircraft*, 1997.

[25] H. A. Gonzalez, G. E. Erickson, B. G. McLachlan, and J. H. Bell, "Effects of various fillet shapes on a 76/40 double delta wing from mach 0.18 to 0.7," in *RTO AVT Symposium*, 2003.

[26] R. Mange and F. Roos, "The aerodynamics of a chined forebody," in *29th AIAA Fluid Dynamics Conference*, 1998.

[27] D. Cohen and R. T. Jones, *High speed wing theory*. Princeton University Press, 2015.

[28] W. P. Henderson, "Effects on wing leading edge radius and reynolds number on logitudinal aerodynamic characteristics of highly swept wing body configurations at subsonic speeds," tech. rep., NASA, 1976.

[29] J. M. Luckring, "Reynoldy number and leading-edge bluntness effects on a 65deg delta wing," in *40th AIAA Aerospace Sciences Meeting & Exhibit*, 2002.

[30] J. M. Luckring, "Compressibility and leading-edge bluntness effects for a 65 delta wing," in *42nd AIAA Aerospace Sciences Meeting & Exhibit*, 2004.

[31] R. T. Jones, "Wing plan forms for high-speed flight," tech. rep., National Advisory Committee for Aeronautics, 1946.

[32] A. Stanbrook and L. C. Squire, "Possible types of flow at swept leading edges," *The Aeronautical Quarterly*, 1964.

[33] E. C. Polhamus, "A concept of the vortex lift of sharp-edge delta wings based on a leading-edge-suction analogy," tech. rep., NASA, 1966.

[34] J. G. Szodruch and D. J. Peake, "Leeward flow over delta wings at supersonic speeds," tech. rep., NASA, 1980.

[35] D. S. Miller and R. M. Wood, "An investigation of wing leading-edge vortices at supersonic speeds," in *AIAA Applied Aerodynamics Conference*, 1983.

[36] S. N. Seshadri and K. Y. Narayan, "Shock-induced separated flows on the lee surface of delta wings," *The Aeronautical Journal*, 1987.

[37] U. Henne, D. Yorita, and C. Klein, "Experimental aerodynamic high speed investigations using pressure-sensitive paint for generic delta wing planforms," *STAB Symposium*, 2018.

[38] T. Liu, J. P. Sullivan, K. Asai, C. Klein, and Y. Egami, *Pressure and temperature sensitive paints - 2nd Edition*. Experimental Fluid Mechanics, 2021.

[39] S. Wiggen and G. Voß, "Vortical flow prediction for the design of a wind tunnel experiment with a pitching

lambda wing," *CEAS Aeronautical Journal*, 2014.

[40] J. Lübker, "Pressure measurements in the dnw-twg perforated test section," tech. rep., DLR Institute for Aeroelasticity, 2014.

[41] S. R. Allmaras and F. T. Johnson, "Modifications and clarifications for the implementation of the spalart-allmaras turbulence model," in *Seventh international conference on computational fluid dynamics*, 2012.

[42] M. L. Shur, P. R. Spalart, M. K. Strelets, and A. K. Travin, "A hybrid rans-les approach with delayed-des and wall-modelled les capabilities," *International journal of heat and fluid flow*, 2008.

[43] M. Rütten and J. Zastrow, "Vortex interaction, vorticity flux and torsion over a generic double-delta wing configuration," in *AIAA AVIATION*, 2022.

[44] J. Neumann, J. Nitzsche, and R. Voss, "Aeroelastic analysis by coupled non-linear time domain simulation," in *AVT-154 specialists meeting on advanced methods in aeroelasticity*, 2008.

[45] M. Ritter, J. Neumann, and W. R. Krüger, "Aeroelastic simulations of high reynolds number aero structural dynamics wind tunnel model," *AIAA Journal*, 2016.

Appendix

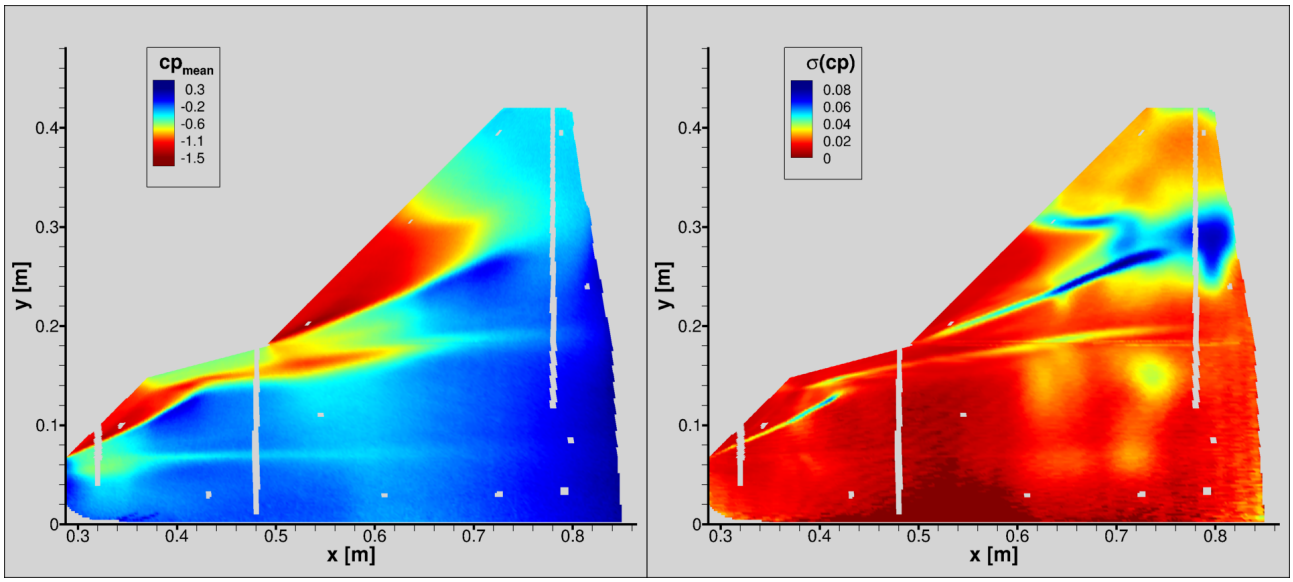

Figure 13 – a: cp_{mean} and $\sigma(cp)$ at Mach-number 0.85 and $\alpha = 9°$, see polar in Fig. 6

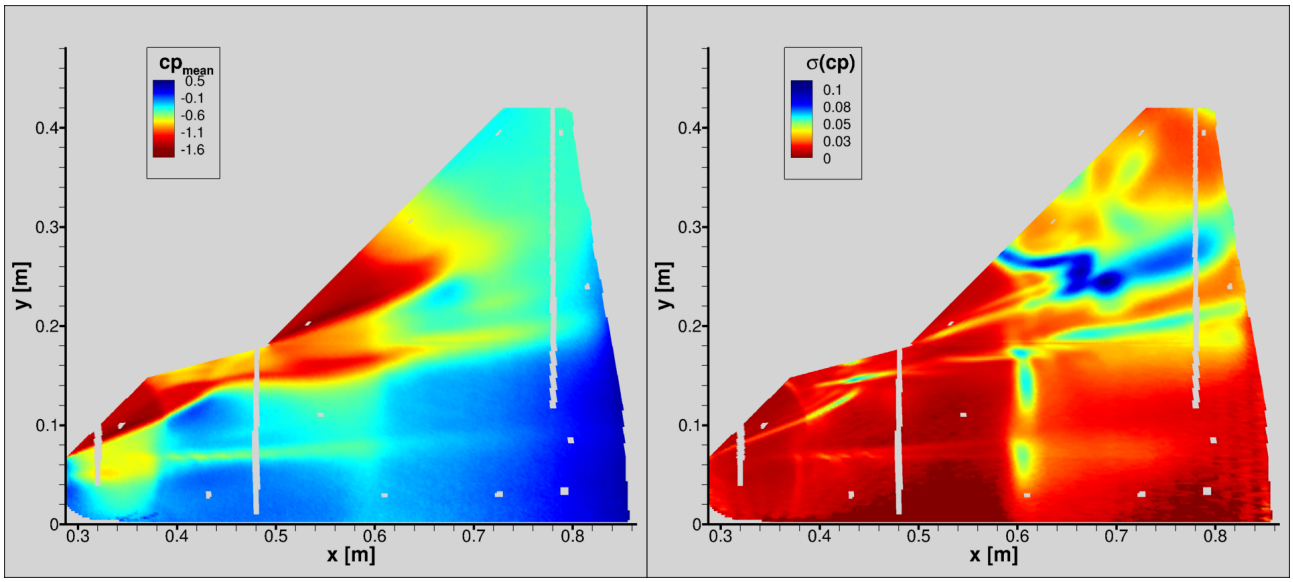

Figure 14 – b: cp_{mean} and $\sigma(cp)$ at Mach-number 0.85 and $\alpha = 12°$, see polar in Fig. 6

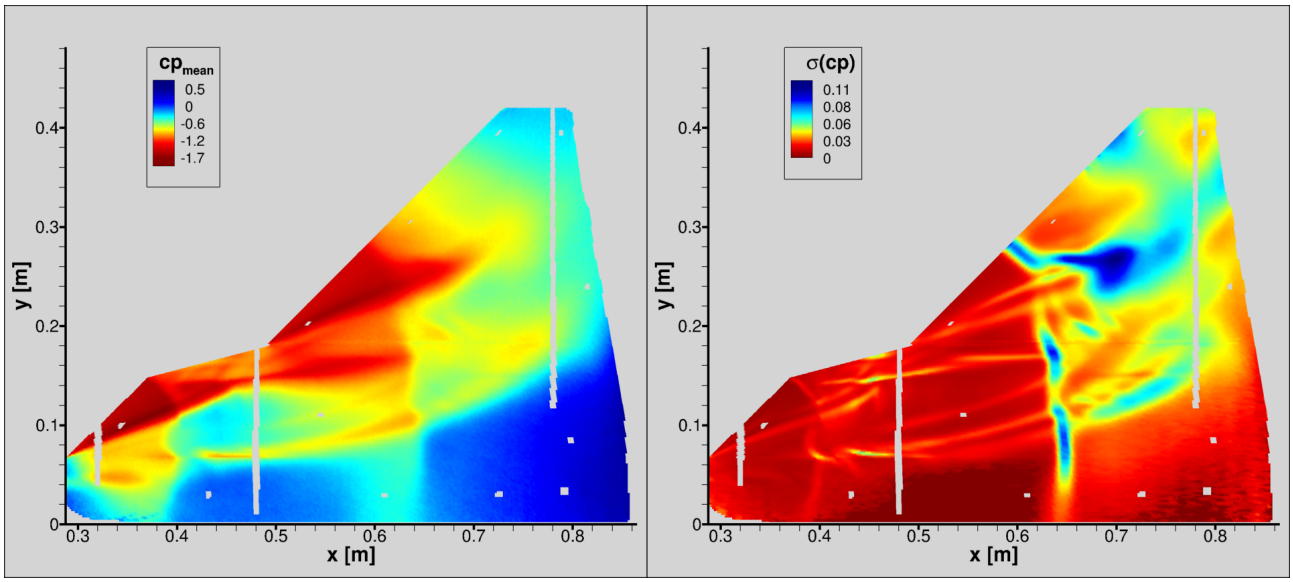

Figure 15 – c: cp_{mean} and $\sigma(cp)$ at Mach-number 0.85 and $\alpha = 15°$, see polar in Fig. 6

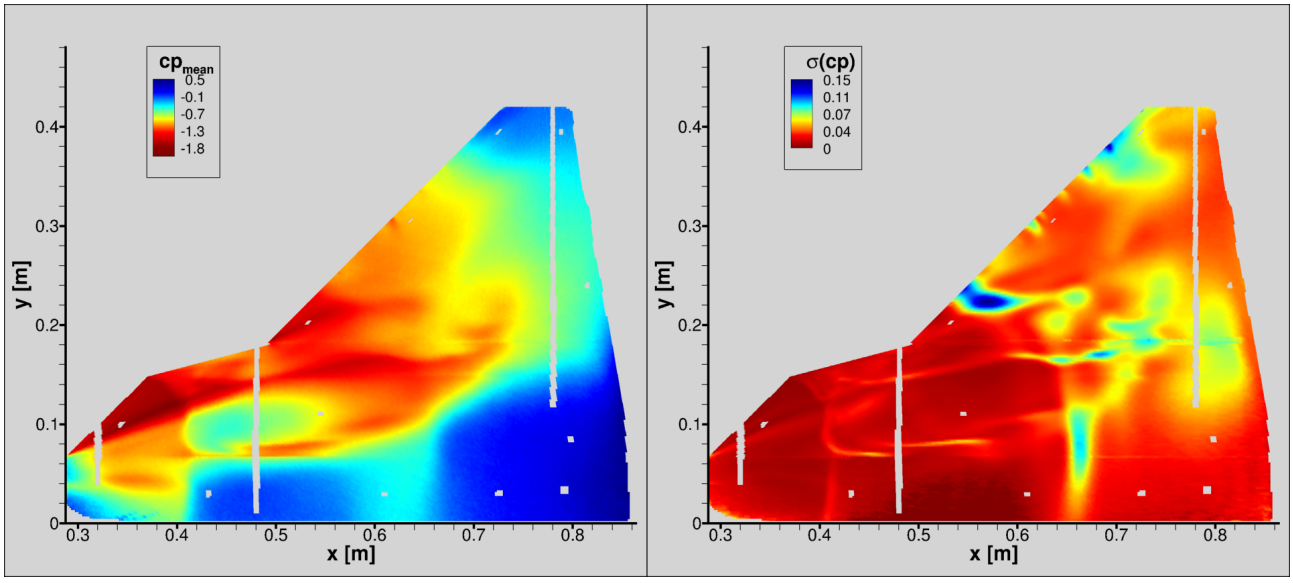

Figure 16 – d: cp_{mean} and $\sigma(cp)$ at Mach-number 0.85 and $\alpha = 18°$, see polar in Fig. 6

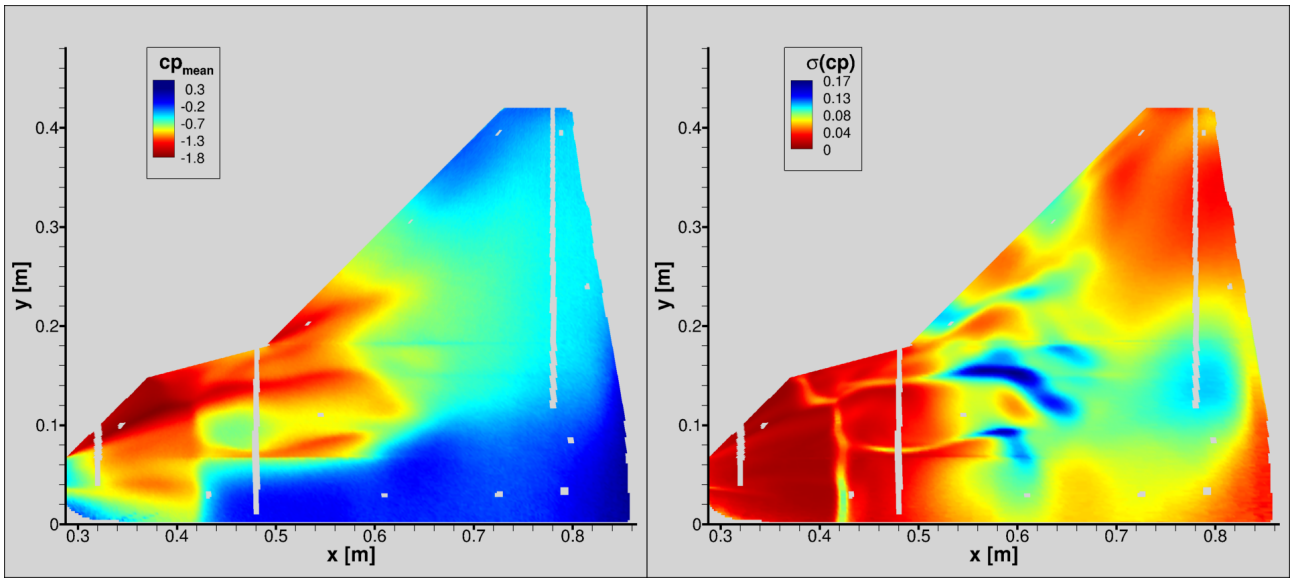

Figure 17 – e: cp_{mean} and $\sigma(cp)$ at Mach-number 0.85 and $\alpha = 21°$, see polar in Fig. 6

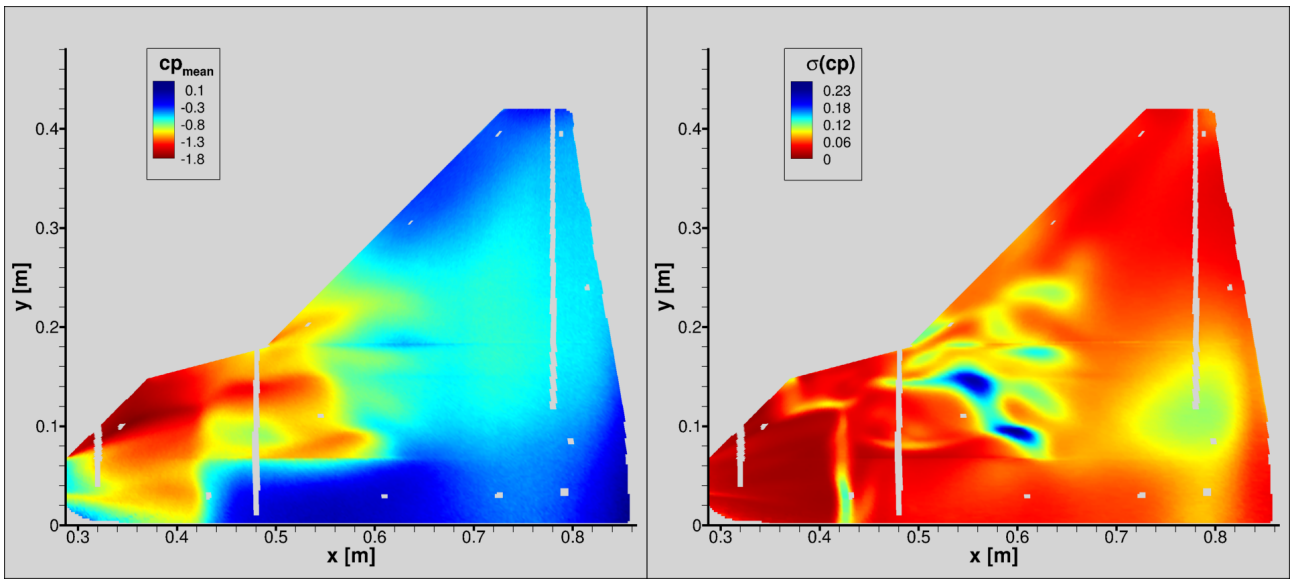

Figure 18 – f: cp_{mean} and $\sigma(cp)$ at Mach-number 0.85 and $\alpha = 24°$, see polar in Fig. 6